
Attenuation Correction Methods Suitable for Brain Imaging with a PET/MRI Scanner: A Comparison of Tissue Atlas and Template Attenuation Map Approaches

Ian B. Malone¹, Richard E. Ansorge¹, Guy B. Williams², Peter J. Nestor³, T. Adrian Carpenter², and Tim D. Fryer²

¹*Cavendish Laboratory, University of Cambridge, Cambridge, United Kingdom;* ²*Wolfson Brain Imaging Centre, Department of Clinical Neurosciences, University of Cambridge, Addenbrooke's Hospital, Cambridge, United Kingdom;* and ³*Neurology Unit, Department of Clinical Neurosciences, University of Cambridge, Addenbrooke's Hospital, Cambridge, United Kingdom*

Modeled attenuation correction (AC) will be necessary for combined PET/MRI scanners not equipped with transmission scanning hardware. We compared 2 modeled AC approaches that use nonrigid registration with rotating ⁶⁸Ge rod-based measured AC for 10 subjects scanned with ¹⁸F-FDG. **Methods:** Two MRI and attenuation map pairs were evaluated: tissue atlas-based and measured templates. The tissue atlas approach used a composite of the BrainWeb and Zubal digital phantoms, whereas the measured templates were produced by averaging spatially normalized measured MR image and coregistered attenuation maps. The composite digital phantom was manually edited to include 2 additional tissue classes (paranasal sinuses, and ethmoidal air cells or nasal cavity). In addition, 3 attenuation values for bone were compared. The MRI and attenuation map pairs were used to generate subject-specific attenuation maps via nonrigid registration of the MRI to the MR image of the subject. SPM2 and a B-spline free-form deformation algorithm were used for the nonrigid registration. To determine the accuracy of the modeled AC approaches, radioactivity concentration was assessed on a voxelwise and regional basis. **Results:** The template approach produced better spatial consistency than the phantom-based atlas, with an average percentage error in radioactivity concentration across the regions, compared with measured AC, of $-1.2\% \pm 1.2\%$ and $-1.5\% \pm 1.9\%$ for B-spline and SPM2 registration, respectively. In comparison, the tissue atlas method with B-spline registration produced average percentage errors of $0.0\% \pm 3.0\%$, $0.9\% \pm 2.9\%$, and $2.9\% \pm 2.8\%$ for bone attenuation values of 0.143 cm^{-1} , 0.152 cm^{-1} , and 0.172 cm^{-1} , respectively. The largest errors for the template AC method were found in parts of the frontal cortex (-3%) and the cerebellar vermis (-5%). Intersubject variability was higher with SPM2 than with B-spline. Compared with measured AC, template AC with B-spline and SPM2 achieved a correlation coefficient (R^2) of 0.99 and 0.98, respectively, for regional radioactivity concentration. The corresponding R^2 for the tissue atlas approach with B-spline registration was 0.98, irrespective of the bone attenuation coefficient. **Conclusion:** Nonrigid registration of joint MRI and attenuation map templates can produce accurate AC for brain PET scans, particularly with measured tem-

plates and B-spline registration. Consequently, these methods are suitable for AC of brain scans acquired on combined PET/MRI systems.

Key Words: attenuation correction; brain; nonrigid registration; PET/MRI scanner

J Nucl Med 2011; 52:1142–1149
DOI: 10.2967/jnumed.110.085076

Attenuation correction (AC) is a vital step in the determination of quantitatively accurate PET images (1). Furthermore, the most commonly used scatter-correction technique (2) also relies on accurate attenuation information. With the advent of scanners that combine PET with MRI (3) and incorporate neither rotating radioactive sources nor CT, a new solution must be found for determining photon attenuation.

It is more challenging to estimate attenuation from MRI than CT because the contrast mechanism is unrelated to photon attenuation. The most obvious approach is to attempt to translate from MRI to attenuation via tissue segmentation (3–8). The greatest difficulty in tissue classification of MRI for AC is that for conventional MRI sequences bone and air appear similar, but bone has the highest attenuation coefficient of any tissue class, whereas air induces negligible photon attenuation. To improve the segmentation of air and bone, Keereman et al. (7) and Catana et al. (8) recently reported the use of ultrashort-echo-time MRI sequences.

The other main approach involves nonrigid registration of an attenuation map produced from a tissue atlas (9) or measured attenuation maps (10–14). In this paper, we compared an AC approach that used a tissue atlas with one that used a measured template attenuation map. Such a comparison has not previously been made on the same patient dataset, and in addition, the methods were tested against the gold standard measured AC with rotating ⁶⁸Ge rod sources rather than singles-mode ¹³⁷Cs transmission scanning (9–11) or CT AC (13,14). The tissue atlas approach used a novel combination of the BrainWeb (15) and Zubal

Received Nov. 10, 2010; revision accepted Mar. 16, 2011.
For correspondence or reprints contact: Richard E. Ansorge, Cavendish Laboratory, JJ Thomson Ave., Cambridge CB3 0HE, U.K.
E-mail: rea1@cam.ac.uk
COPYRIGHT © 2011 by the Society of Nuclear Medicine, Inc.

digital phantoms (16), with 3 variants produced through the use of different attenuation coefficients for bone. For non-rigid registration, the cubic B-spline free-form deformation algorithm of Rueckert et al. (17) implemented in the vtkCISG toolkit (18) was used in addition to SPM2 (www.fil.ion.ucl.ac.uk/spm), which had previously been applied to this problem. Another novel aspect was the use of a pseudo-MR image for registration with the tissue atlas approach.

The methods were applied to ^{18}F -FDG scans of 10 subjects. Both regional and voxelwise analysis was applied to assess the accuracy of the techniques.

MATERIALS AND METHODS

Generation of MRI and Attenuation Map Atlas Pair Using a Tissue Atlas

To assign attenuation coefficients to tissue classes of the BrainWeb phantom (15), mass attenuation coefficients and reference densities from Report 44 of the International Commission on Radiation Units and Measurements (19) were used, together with updated values from Hubbell and Seltzer (20). The resulting values are shown in Table 1. The BrainWeb phantom is based on fuzzy clustering of T1-weighted MR images and manual segmentation, leading to regions within the head that are classed as bone, based on low signal and location, but that are in fact air-filled or a mixture of bone and air. Consequently, we found it necessary to add 2 additional classes: paranasal sinuses assigned with the attenuation coefficient of air, and an ethmoidal air cell or nasal cavity class. The attenuation coefficient for the ethmoidal air cell or nasal cavity region was found by taking the average within a region of interest (ROI) encompassing these structures in measured attenuation maps of 10 subjects. The changes made to the BrainWeb phantom, aided by reference to a head and neck atlas (21), are shown in Supplemental Figure 1 (supplemental materials are available online only at <http://jnm.snmjournals.org>).

Bones are composed of cortical and cancellous parts. The maximum attenuation coefficient is that of cortical bone, with a value of approximately 0.172 cm^{-1} for 511-keV photons (22,23).

TABLE 1

Linear Attenuation Coefficients (μ) and T1-Weighted MRI Intensities Assigned to BrainWeb Tissue Classes

Class	μ (cm^{-1})	MRI
Background (air)	0.000105	500
Cerebrospinal fluid	0.097000	4,200
Gray matter	0.100000	10,000
White matter	0.100000	11,000
Fat	0.092000	13,000
Muscle or skin	0.100000	8,000
Skin	0.100000	5,000
Skull	*	1,500
Connective tissue	0.100000	2,000
Paranasal sinuses	0.000105	1,000
Ethmoidal air cells or nasal cavity	0.066000	3,300

*The skull was attributed three attenuation coefficient values (0.143 cm^{-1} , 0.152 cm^{-1} , and 0.172 cm^{-1}), as described in the text.

As we can only infer the presence of bone in T1-weighted MR images, an estimate for the density must be provided; without the ability to measure density directly, the choice must necessarily result in a compromise between over- and underestimates in different regions. The average bone density described by White et al. (24) gives an attenuation coefficient of 0.143 cm^{-1} , as used by Zaidi et al. (4). The average of the survey of literature values in Zaidi et al. (4) is 0.152 cm^{-1} . We tested AC accuracy using all 3 values, and henceforth these 3 options will be referred to as A143, A152, and A172 (bone attenuation coefficient 0.143 cm^{-1} , 0.152 cm^{-1} , and 0.172 cm^{-1} , respectively).

Tissue class MRI values were chosen by comparison with a T1-weighted MR image and are also shown in Table 1. The exact values are scan-dependent, but the normalized mutual information cost function used for registration is robust to unequal contrast.

The BrainWeb phantom has dimensions of $180 \times 220 \times 221\text{ mm}$ with 1 mm^3 voxels. When registered to patient MR images, the phantom does not always cover the full PET axial field of view (FOV). To extend the phantom to cover the FOV (153 mm), the BrainWeb phantom was combined with the CT-based Zubal head phantom (16). Because the Zubal phantom has thicker slices (5 mm) than the MRI-based BrainWeb phantom, attempting to use it alone results in poor registration along edges parallel to transverse planes, and the thick slices cause such edges to be less detailed. Instead, we registered the Zubal phantom to the BrainWeb phantom by first converting Zubal anatomic labels to BrainWeb tissue classes, then generating pseudo-MRI volumes from both phantoms, and lastly applying an affine followed by a nonlinear registration using vtkCISG (Supplemental Fig. 2). The phantom combination process is shown in Supplemental Figure 3A.

Generation of Measured Template MRI and Attenuation Map Pair

The major drawback to producing an attenuation map from a tissue atlas is the need to make assumptions about the attenuation coefficients, particularly for bone. An alternative method is to use coregistered measured attenuation maps and MR images to create the template pair. This approach has been previously applied by Kops and Herzog (12).

We created the template pair from PET and MR images of 10 control subjects who took part in an ^{18}F -FDG dementia study (25). The T1 MRI data were acquired on a 3T Bruker scanner (Bruker BioSpin) with a spoiled gradient-recalled sequence having the following parameters: echo time, 5 ms; repetition time, 19.1 ms; FOV, $25.6 \times 22.0 \times 18.0\text{ cm}$; and matrix size, $256 \times 256 \times 256$. PET data were acquired using an Advance scanner (GE Healthcare), with a 10-min preinjection transmission scan obtained using rotating ^{68}Ge rods. For each subject, the corresponding blank ^{68}Ge scan was acquired for 60 min.

For each subject, the measured attenuation map was coregistered and resliced to the MR image using SPM5. The individual MR images were registered to the BrainWeb-based MRI volume using SPM2, which applies full affine followed by nonlinear registration, or vtkCISG to perform rigid registration and scaling, followed by full affine, and then nonlinear B-spline registration. For all registration steps, normalized mutual information (26) was used as the registration measure.

For each subject, binary masks of the PET and MRI FOVs were warped to BrainWeb space with the same parameters as the attenuation map and MR image. This enabled each voxel value of the measured templates to be obtained by averaging only those

subjects with a corresponding nonzero warped mask value. Finally, the object extractor tool in Analyze (AnalyzeDirect) was used to remove attenuation outside the head due to the bed and head holder. The template creation process is summarized in Supplemental Figure 3B.

Generation of a Subject-Specific Attenuation Map

The derivation of a subject-specific attenuation map using either the tissue atlas method or the template method is shown in Supplemental Figure 3C. First, the atlas or template MR image was nonrigidly registered to the subject MR image using vtkCISG and, for the template method, SPM2. The derived transformation was then used to transform the coregistered atlas or template attenuation map into subject MRI space. For the atlas-based approach, the attenuation map was smoothed with a gaussian filter of 6 mm full width at half maximum to approximate the resolution of measured attenuation. The subject MR image was then coregistered to a mean ^{18}F -FDG image (35–55 min after injection) using normalized mutual information–based affine registration in SPM5. The resulting affine transformation was used to transform the atlas or template attenuation map from subject MRI space to subject PET space. Finally, the patient bed and head holder were added to the atlas or template attenuation map in PET space, for which the bed and head holder attenuation were determined from a separate hour-long ^{68}Ge transmission scan.

Image Reconstruction with Subject-Specific AC

The details of the PET data acquisition have been described previously (25). Briefly, each subject was injected with approximately 74 MBq of ^{18}F -FDG. Emission data were acquired in a dynamic sequence for 55 min after injection, and a mean ^{18}F -FDG image was produced using decay-corrected data from 35 to 55 min after injection, the time period used previously to determine glucose metabolic rate with the autoradiographic technique (25).

Image reconstruction using the various attenuation maps was made possible through the use of the breakpointing feature on the Advance scanner. For the 3-dimensional filtered backprojection algorithm installed on the scanner (27), this feature allows for stopping and restarting of the data correction process before the filtering steps. Hence, just before the AC steps (2 are applied: 1 for the initial 2-dimensional image and then 1 for the final 3-dimensional image), the reconstruction process was halted and an atlas

or template AC sinogram was imported. The reconstruction pipeline was then restarted. The AC sinograms were generated by forward projecting the PET space attenuation map into the 2-dimensional sinogram geometry of the Advance by using length-of-intersection ray tracing and by taking the exponent of the attenuation line integrals. For reconstructions using the measured transmission scan, the reconstruction process was allowed to run without interruption.

Assessment of Atlas or Template AC

Regional Quantification. Standard-space ROIs were applied to the mean ^{18}F -FDG images by normalizing the T1-weighted MR images, and hence the coregistered ^{18}F -FDG images, to the International Consortium for Brain Mapping ICBM152 T1 MRI template (28) using the unified segmentation tool in SPM5. ROIs were defined using the WFU PickAtlas SPM toolbox (29). Two levels of detail were used: the Talairach Daemon (TD) hemispheres (7 ROIs) and the TD labels (110 ROIs) listed in Supplemental Table 1.

Voxelwise Assessment. To test for statistically significant voxelwise differences between the aforementioned mean ^{18}F -FDG images ($n = 10$) reconstructed with modeled and measured AC, paired t tests were performed using SPM5. The preliminary steps were the same as for the ROI analysis: normalization of the ^{18}F -FDG images to standard space using the patient MR image. A 4-mm isotropic gaussian kernel was then applied. To provide information on both significant underestimation and significant overestimation of radioactivity concentration using modeled AC, for each comparison of image sets two 1-sided tests ($P < 0.025$) were conducted rather than a single 2-sided test. Variances were set to be equal, and to avoid eliminating differences due to overall scaling factors, grand mean scaling was not applied. Data rate correction was not used, to avoid suppressing differences.

RESULTS

Atlas or Template Pairs

The joint atlas or template pairs produced using vtkCISG registration are illustrated in Figure 1. Although those produced from the tissue atlas approach have higher resolution, after nonrigid registration to the subject MR image the warped tissue atlas attenuation map is smoothed, and the

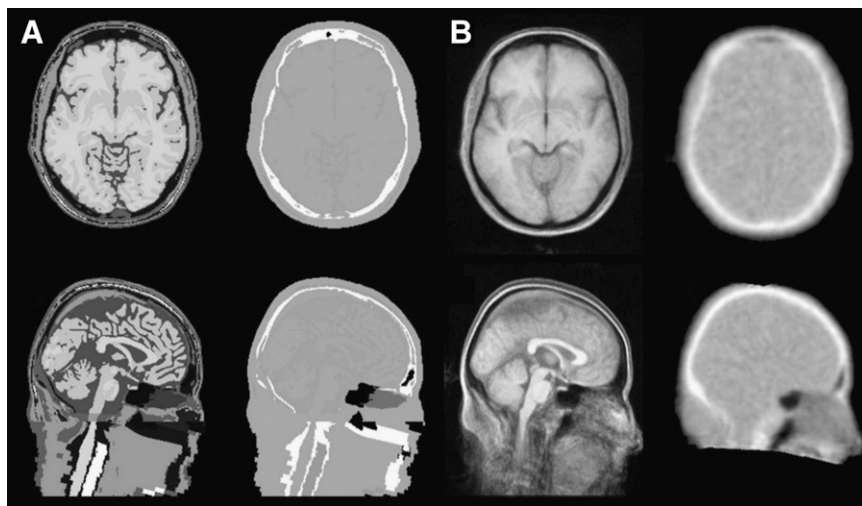


FIGURE 1. Transverse and sagittal sections through MRI and attenuation maps generated from the tissue atlas (A) and measured templates created using vtkCISG registration (B).

subject-specific attenuation maps from both approaches should therefore have similar resolution.

Comparison of Modeled and Measured Attenuation Maps

The voxelwise correlation of attenuation coefficient between the modeled (vtkCISG registration) and measured attenuation maps is shown for 1 subject in Figure 2. Voxels for which the measured attenuation coefficient was less than that of air ($1.05 \times 10^{-4} \text{ cm}^{-1}$) were excluded. The higher noise level of the measured maps resulted in the horizontal bands, particularly for the noise-free tissue atlas methods. At low measured attenuation values, there was some overestimation by the modeled AC approaches. These voxels correspond to those in the vicinity of internal air spaces or the outer surface of the skull, and the discrepancy could be due to registration errors or resolution differences.

Correlation of Radioactivity Concentration Reconstructed with Modeled and Measured AC

Illustrative image planes for reconstruction with modeled (vtkCISG registration) and measured AC are given for 1 subject in Figure 3. There are no visibly discernible differences between measured and template AC, but the A143 tissue atlas underestimated AC of the frontal cortex near the sinuses (marked with an arrow).

Table 2 summarizes the head-masked voxelwise correlation statistics across the 10 subjects. For vtkCISG registration, A152 achieved the closest correlation to unity of the atlas-based methods, but a better correlation was achieved by template AC, which also had the highest correlation

coefficient for ROIs. For template AC, SPM2 registration produced lower correlations than vtkCISG that were also more variable across subjects.

Table 3 compares the correlations found in this study with those of other MRI-based AC methods reported in the literature. All these correlations are groupwise—that is, all ROI data from all subjects were used to determine a single correlation coefficient—and are for ^{18}F -FDG, so differences in the correlations are not due to the use of different tracers. The correlations found in this study were higher than any previously published, and the correlation for template AC using vtkCISG registration is shown in Figure 4.

Regional and Voxelwise Differences in Radioactivity Concentration Between Modeled and Measured AC

To determine regional differences, we investigated the percentage change in the ROI radioactivity concentration with modeled AC, compared with that observed with measured AC (Table 4; Supplemental Table 1). The distribution of differences for TD labels (Supplemental Table 1) showed that the template AC method with vtkCISG registration was more consistent across the ROI set as a whole, with only 4 of the 110 ROIs having absolute errors greater than 3%. For template AC with SPM2, A143, A152, and A172, the number of ROIs with absolute errors greater than 3% was 18, 38, 39, and 61, respectively, and average percentage errors of $-1.2\% \pm 1.2\%$, $-1.5\% \pm 1.9\%$, $0.0\% \pm 3.0\%$, $0.9\% \pm 2.9\%$, and $2.9\% \pm 2.8\%$ were found for template (vtkCISG), template (SPM2), A143, A152, and A172 AC, respectively. The largest errors for the template approach with vtkCISG

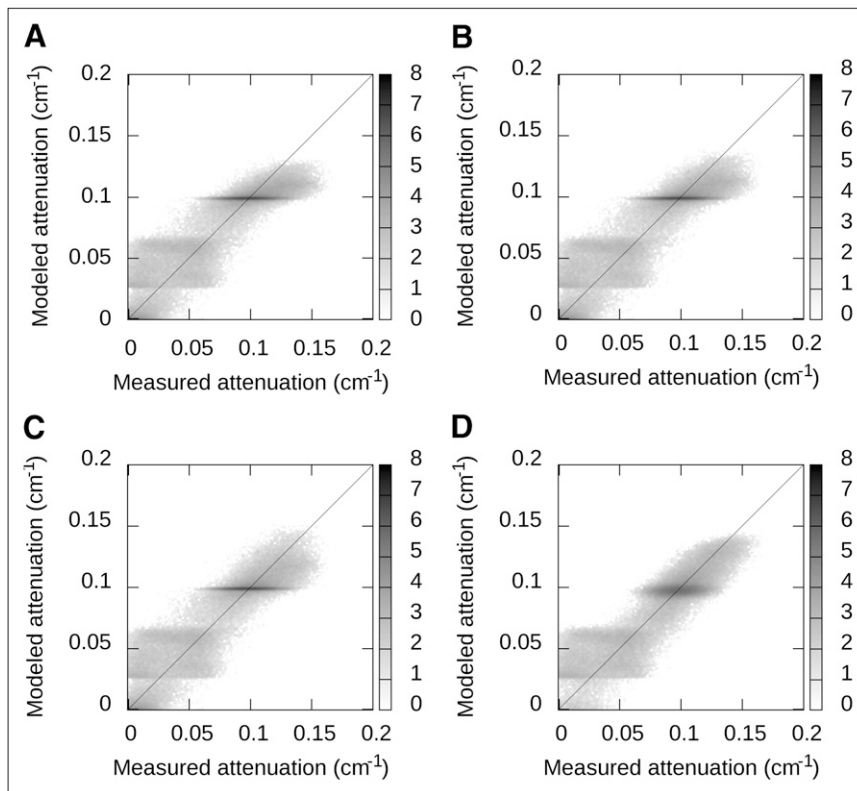


FIGURE 2. Joint histograms of attenuation coefficients for measured attenuation maps and those modeled with A143 (A), A152 (B), A172 (C), and measured template using vtkCISG registration (D). Data are for single subject, and intensity scale is logarithm of number of voxels per bin, where bins are 10^{-3} cm^{-1} wide.

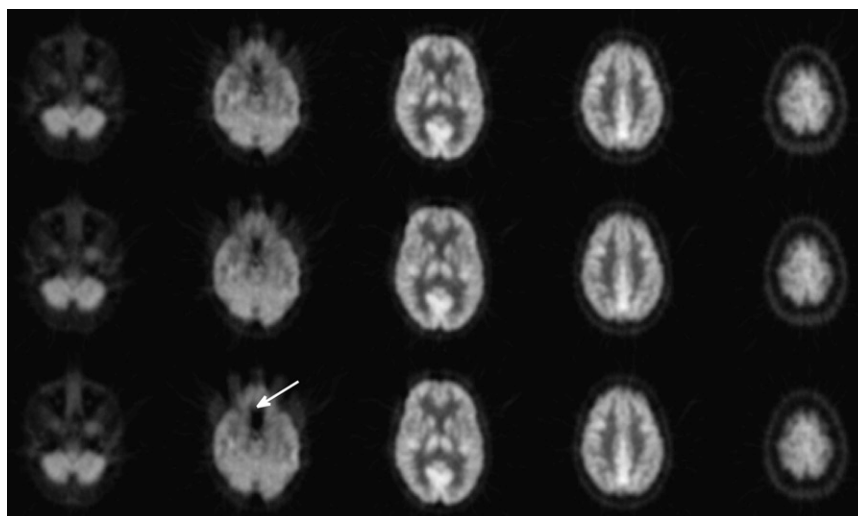


FIGURE 3. Transverse ^{18}F -FDG images for 1 subject with AC from measured transmission scan (top), template using vtkCISG registration (middle), and A143 (bottom). Arrow points to most discernible difference between images. Linear grayscale has threshold of 10 kBq/mL applied.

registration were in the pyramis vermis (left, -5.5% ; right, -3.9%), which is a small structure. The rest of the vermis was less strongly affected.

Template AC with SPM2 registration produced the largest intersubject variability per region (Supplemental Table 1), with the gyrus rectus notable for a relatively large intersubject variability for all methods. This region was also subject to the largest underestimation in radioactivity concentration for the tissue-atlas methods, perhaps because the attenuation coefficient of the neighboring ethmoidal air cells or nasal cavity was an underestimate due to partial-volume error in the measured attenuation maps from which it was obtained, and/or perhaps because of the use of a single attenuation coefficient for this heterogeneous region.

Results for the voxelwise paired t test comparison between mean ^{18}F -FDG images using template (vtkCISG registration) and measured AC are shown in Supplemental Figure 4. The largest cluster of underestimation with the template AC method was in the frontal cortex.

DISCUSSION

AC is a vital data correction if quantitatively accurate images are required. In addition, attenuation maps are used

for the most commonly applied scatter-correction technique, single-scatter modeling (2). Unless rotating radioactive sources or a CT scanner is incorporated, combined PET/MRI scanners will have to use modeled AC rather than directly measured AC. A rotating rod source mechanism could be incorporated, but as PET/MRI systems will primarily be designed for whole-body imaging, with a patient aperture of 70 cm desirable for radiotherapy planning applications, rod sources are unlikely to be included as the limited achievable bore diameter of the MR magnet means that the PET detector/gradient coil assembly is likely to be flush with the surface of the patient port. For brain imaging on a whole-body PET/MRI system, there will be space available for a rotating source between the receive coil and the patient port, but if an alternative solution can be found (such as those examined in this paper), it is unlikely that these scanners will be fitted with a removable rotating rod source mechanism purely for brain imaging. Consequently, in this study we have compared 2 methods employing nonrigid registration for AC of brain studies against gold standard AC using geometrically windowed rotating ^{68}Ge rods.

The approach based on a measured template attenuation map produced from a group of 10 subjects provided

TABLE 2
Correlation Coefficients and Regression Values (Mean \pm SD for 10 Subjects) for Radioactivity Concentration Reconstructed with Modeled and Measured AC

Method	AC method	R^2	Slope	Intercept (Bq/mL)
Voxelwise	A143 (vtkCISG)	0.977 ± 0.005	0.993 ± 0.022	-0.005 ± 0.030
	A152 (vtkCISG)	0.977 ± 0.005	1.001 ± 0.022	-0.001 ± 0.031
	A172 (vtkCISG)	0.974 ± 0.005	1.018 ± 0.022	0.010 ± 0.033
	Template (vtkCISG)	0.986 ± 0.005	0.981 ± 0.022	0.007 ± 0.026
	Template (SPM2)	0.979 ± 0.024	0.979 ± 0.033	0.003 ± 0.034
TD labels	A143 (vtkCISG)	0.945 ± 0.021	0.980 ± 0.041	0.104 ± 0.154
	A152 (vtkCISG)	0.947 ± 0.021	0.989 ± 0.042	0.103 ± 0.152
	A172 (vtkCISG)	0.948 ± 0.022	1.009 ± 0.044	0.101 ± 0.151
	Template (vtkCISG)	0.971 ± 0.019	0.973 ± 0.057	0.096 ± 0.210
	Template (SPM2)	0.938 ± 0.116	0.935 ± 0.095	0.247 ± 0.310

TABLE 3

Groupwise Correlation Between Modeled and Measured AC in Literature and from This Study

Method	¹⁸ F-FDG parameter	R ²	Subjects (n)	ROIs per subject
Direct segmentation (4)*	Cerebral glucose metabolic rate	0.91	10	20
Zubal tissue atlas (9)*	Cerebral glucose metabolic rate	0.84	10	20
Measured template (11)*	Radioactivity concentration	0.91	9	63
Measured templates (30)†	Radioactivity concentration	0.91–0.94	15	12
BrainWeb–Zubal atlas†	Radioactivity concentration (vtkCISG)	0.98	10	110
Measured template†	Radioactivity concentration (vtkCISG)	0.99	10	110
	Radioactivity concentration (SPM2)	0.98	10	110

*Compared with singles-mode ¹³⁷Cs transmission scanning.

†Compared with coincidence-mode ⁶⁸Ge transmission scanning.

results superior to the approach using a digital phantom–based attenuation map. The marginal superiority of the template approach could be due to the fact that the template is based on data from multiple subjects, whereas the BrainWeb (15) and Zubal (16) phantoms are based on single subjects, and a multisubject source may warp to the target subject more reliably than one based on a single subject. The template is also constructed from measured data, whereas for the tissue atlas approach attenuation coefficients need to be ascribed to the tissue classes. The main problem with the latter is the value to use for bone; 3 values were tried but none produced results as good as template AC.

The superiority of template AC over AC modeled from a digital phantom is in agreement with a comparison of the

results found by Zaidi et al. (9) and Montandon and Zaidi (11). The difference between these approaches, however, was less than that found between the 2 studies of Zaidi et al. One explanation is the difference between the digital phantoms used, with Zaidi et al. (9) using the Zubal phantom and this work using a modified version of the BrainWeb phantom combined with the Zubal phantom for the neck and oral cavity.

Compared with the gold standard measured AC, radioactivity concentrations with template AC using vtkCISG registration were underestimated by approximately 1% on average. This small error could be due to registration error, differences in the resolution of the modeled and measured attenuation maps, and/or small differences in how the AC factors are calculated through forward projection of the attenuation maps. The error compared with measured AC was more variable across the brain for tissue atlas–based AC than template AC, with more positive errors being found as the bone attenuation value was increased.

The correlations found for radioactivity concentration between modeled and measured AC are higher in this study than previously reported (Table 3). The correlations reported by Zaidi et al. (4,9) and Montandon and Zaidi (11) were through comparison with singles-mode ¹³⁷Cs transmission scanning, which cannot be considered to be as much a gold standard as the coincidence-mode ⁶⁸Ge transmission scanning used in this study and by Kops and Herzog (30). The correlations found in this study for template AC using SPM2 are higher than those reported by Kops and Herzog using the same approach. Our higher correlations could be due to the fact that Kops and Herzog applied separate spatial normalization to the MR images and attenuation maps to generate their templates, whereas we coregistered each attenuation map to the corresponding MR image and thus used MRI-based spatial normalization, and/or they could be due to the fact that the scatter-correction methods had differential dependence on the attenuation information.

Nonrigid registration with the Rueckert B-spline algorithm implemented in vtkCISG produced results superior to SPM2, consistent with a comparison of brain spatial normalization algorithms by Klein et al. (31). Because other algo-

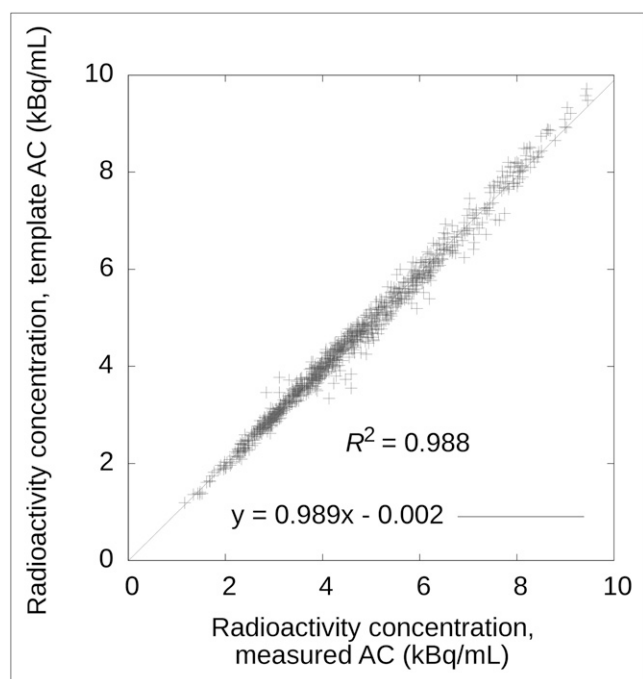


FIGURE 4. Correlation of regional (TD labels) radioactivity concentration reconstructed with template (vtkCISG registration) and measured AC using data from 10 subjects (1,100 data points).

TABLE 4
Average Percentage Change (Mean \pm SD) in Reconstructed Radioactivity Concentration with Modeled Versus Measured AC Across All Subjects

Region	vtkCISG				SPM2 template
	A143	A152	A172	Template	
Left brain stem	2.3 \pm 0.8	2.7 \pm 0.8	3.6 \pm 0.8	-1.6 \pm 0.7	-1.0 \pm 2.4
Right brain stem	2.1 \pm 0.8	2.5 \pm 0.8	3.4 \pm 0.8	-1.3 \pm 0.7	-0.8 \pm 2.5
Left cerebellum	-1.6 \pm 0.7	-0.6 \pm 0.7	1.6 \pm 0.6	-1.1 \pm 0.7	-1.2 \pm 3.7
Right cerebellum	-1.5 \pm 0.9	-0.6 \pm 0.9	1.6 \pm 0.9	-1.3 \pm 0.9	-1.0 \pm 3.9
Left cerebrum	-0.1 \pm 0.7	0.7 \pm 0.7	2.6 \pm 0.7	-1.7 \pm 0.6	-1.6 \pm 3.2
Right cerebrum	0.2 \pm 0.8	1.0 \pm 0.8	2.9 \pm 0.7	-0.9 \pm 0.7	-1.9 \pm 3.3
Interhemispheric	-2.2 \pm 0.7	-1.4 \pm 0.7	0.3 \pm 0.8	-2.0 \pm 0.7	-2.1 \pm 3.5

gorithms were found to be superior to the Rueckert algorithm in Klein et al., at least for registration of the brain, further improvements in the nonrigid registration may be possible.

At the regional level, for template AC the greatest discrepancies, compared with measured AC, were found in the vermis and semilunar lobule of the cerebellum, and the dorsolateral prefrontal cortex. These findings were substantiated by voxelwise analysis. Errors in the cerebellum have implications for methods that normalize to the cerebellum signal or use the cerebellum as a reference tissue (32). However, the cerebellum as a whole had a level of error similar to that of the cerebrum (Table 4). The highest regional variability was found in the orbital surface of the frontal cortex. These regions will be heavily influenced by the accuracy of the attenuation modeling in the sinuses. The intersubject variability in these regions and the inability of the nonrigid algorithm to perfectly correct for this is the likely cause of the relatively high variability.

The relevance of regional differences and variability will depend on the regions under examination. For instance, the variability in parts of the frontal cortex will reduce the ability to detect significant changes between groups or subjects such as in studies of frontotemporal dementia. In contrast, the much lower variability in centrally located structures such as the caudate and thalamus is beneficial for imaging tracers when these regions are of interest, for example, striatal imaging with the dopamine D₂/D₃ receptor antagonist ¹¹C-raclopride.

The results produced by template AC using vtkCISG registration in this study compare favorably with other MRI-based AC methods. AC based on direct segmentation of T1-weighted MRI (5), compared with measured AC with ⁶⁸Ge rods, gave an average regional error for ¹⁸F-FDG of -3.2% \pm 0.9% (6), compared with -1.2% \pm 1.2% found in this study. Using a combination of nonrigid registration of an atlas CT and pattern-recognition techniques, Hofmann et al. (14) reported errors of -3.2% \pm 2.5%, although that study used comparison with CT-based AC, which, like ¹³⁷Cs transmission scanning, cannot be regarded as a gold standard AC measurement. Average errors on the order of 5%, compared with CT-based AC, were recently reported

by Keereman et al. (7) for segmentation of a fast transverse relaxation rate map derived from an ultrashort-echo-time sequence.

For the tissue atlas and template AC methods, other attenuating objects (bed and head holder) were added to the patient-specific attenuation map. For simultaneous PET/MRI, there will also be attenuation due to materials associated with the MR image acquisition, namely the receiver and gradient coils. Catana et al. (8) demonstrated that ignoring the latter materials can lead to errors of up to 50%. For brain imaging, it is possible for the MRI equipment that lies between the patient and the PET detectors (i.e., transmit-receive coil and possibly gradient coils) to have a fixed geometry; this would be possible for a bird cage coil, the most commonly used transmit-receive coil for brain MRI. A fixed geometry would also result in invariant attenuation from the bed. The attenuation of the coils and bed, determined using ⁶⁸Ge transmission scanning when possible or through use of reference attenuation coefficients for their composite materials, could be combined to produce a standard attenuation map, with smoothing applied if necessary to match the PET resolution. For each scan, the attenuation due to the patient, estimated using either the measured template or tissue-atlas approach, matched to the PET resolution could then be added to the standard attenuation map. AC factors would then be determined by forward projecting through the attenuation map and taking the exponent of the resulting attenuation line integrals.

The template AC method described in this study was used for AC on the same scanner that acquired the data from which the template was formed, but this will not be possible for a PET/MRI scanner. This limitation will have an impact on the relative resolution of the attenuation and emission data. Matching the resolution is considered the optimal choice, as is performed for CT-based AC for which the segmented and scaled CT map is smoothed to the resolution of the PET before forward projection. Ideally, the data used to form the measured template attenuation map should be acquired on a scanner with a resolution and axial FOV similar to the PET detector array in the PET/MRI scanner.

Finally, in this work the vtkCISG nonrigid registrations typically required about 1 h on a 32-node 2.8-GHz Xeon (Intel) cluster. However, recent advances using graphic processing units have shown that such registrations can now be done in a few minutes on a single desktop personal computer (33).

CONCLUSION

This study conducted the first, to our knowledge, comparison in the same dataset of tissue atlas and template AC approaches with gold standard measured AC using rotating ^{68}Ge rods. The template AC approach with vtkCISG B-spline nonrigid registration outperformed both template AC with SPM2 nonrigid registration and the tissue atlas method for spatial consistency across the brain. In addition, vtkCISG registration produced results superior to SPM2 in terms of intersubject variability.

The correlations between template AC and measured AC were higher than values reported for other methods that could be used for AC of brain studies on a PET/MRI scanner. Regional percentage errors in radioactivity concentration ($\sim 1\%$) also compared well with those reported for these other methods. Template AC and, to a lesser extent, tissue atlas-based AC are attractive options for AC of brain scans acquired on combined PET/MRI systems.

DISCLOSURE STATEMENT

The costs of publication of this article were defrayed in part by the payment of page charges. Therefore, and solely to indicate this fact, this article is hereby marked “advertisement” in accordance with 18 USC section 1734.

ACKNOWLEDGMENTS

This study was supported by a studentship from the Engineering and Physical Sciences Research Council (EPSRC) and the Higher Education Funding Council for England (HEFCE). The data used in this study were acquired as part of a Medical Research Council (MRC) Programme grant (G9724461). No other potential conflict of interest relevant to this article was reported.

REFERENCES

1. Huang SC, Hoffman EJ, Phelps ME, Kuhl DE. Quantitation in positron emission computed tomography: 2. Effects of inaccurate attenuation correction. *J Comput Assist Tomogr.* 1979;3:804–814.
2. Watson CC, Newport D, Casey ME, deKemp RA, Beanlands RS, Schmand M. Evaluation of simulation-based scatter correction for 3-D PET cardiac imaging. *IEEE Trans Nucl Sci.* 1997;44:90–97.
3. Schlemmer HP, Pichler BJ, Schmand M, et al. Simultaneous MR/PET imaging of the human brain: feasibility study. *Radiology.* 2008;248:1028–1035.
4. Zaidi H, Montandon ML, Slosman DO. Magnetic resonance imaging-guided attenuation and scatter corrections in three-dimensional brain positron emission tomography. *Med Phys.* 2003;30:937–948.
5. Wagenknecht G, Kops ER, Tellmann L, Herzog H. Knowledge-based segmentation of attenuation-relevant regions of the head in T1-weighted MR images for attenuation correction in MR/PET systems. *IEEE Nucl Sci Symp Conf Rec.* 2009;3338–3343.

6. Kops ER, Wagenknecht G, Scheins J, Tellmann L, Herzog H. Attenuation correction in MR-PET scanners with segmented T1-weighted MR images. *IEEE Nucl Sci Symp Conf Rec.* 2009;2530–2533.
7. Keereman V, Fierens Y, Broux T, De Deene Y, Lonnew M, Vandenberghe S. MRI-based attenuation correction for PET/MRI using ultrashort echo time sequences. *J Nucl Med.* 2010;51:812–818.
8. Catana C, van der Kouwe A, Benner T, et al. Toward implementing an MRI-based PET attenuation-correction method for neurologic studies on the MR-PET brain prototype. *J Nucl Med.* 2010;51:1431–1438.
9. Zaidi H, Montandon ML, Slosman DO. Attenuation compensation in cerebral 3D PET: effect of the attenuation map on absolute and relative quantitation. *Eur J Nucl Med Mol Imaging.* 2004;31:52–63.
10. Montandon ML, Zaidi H. Atlas-guided non-uniform attenuation correction in cerebral 3D PET imaging. *Neuroimage.* 2005;25:278–286.
11. Montandon ML, Zaidi H. Quantitative analysis of template-based attenuation compensation in 3D brain PET. *Comput Med Imaging Graph.* 2007;31:28–38.
12. Kops ER, Herzog H. Alternative methods for attenuation correction for PET images in MR-PET scanners. *IEEE Nucl Sci Symp Conf Rec.* 2007: 4327–4330.
13. Schreiber E, Nye JA, Schuster DM, Martin DR, Votaw J, Fox T. MR-based attenuation correction for hybrid PET-MR brain imaging systems using deformable image registration. *Med Phys.* 2010;37:2101–2109.
14. Hofmann M, Steinke F, Scheel V, et al. MRI-based attenuation correction for PET/MRI: a novel approach combining pattern recognition and atlas registration. *J Nucl Med.* 2008;49:1875–1883.
15. Collins DL, Zijdenbos AP, Kollokian V, et al. Design and construction of a realistic digital brain phantom. *IEEE Trans Med Imaging.* 1998;17:463–468.
16. Zubal IG, Harrell CR, Smith EO, Rattner Z, Gindi G, Hoffer PB. Computerized 3-dimensional segmented human anatomy. *Med Phys.* 1994;21:299–302.
17. Rueckert D, Sonoda LI, Hayes C, Hill DLG, Leach MO, Hawkes DJ. Nonrigid registration using free-form deformations: application to breast MR images. *IEEE Trans Med Imaging.* 1999;18:712–721.
18. Hartkens T, Rueckert D, Schnabel JA, Hawkes DJ, Hill DLG. VTK CISG registration toolkit: an open source software package for affine and non-rigid registration of single and multimodal 3D images. Leipzig: Springer-Verlag; 2002.
19. *Tissue Substitutes in Radiation Dosimetry and Measurement, ICRU Report 44.* Bethesda, MD: International Commission on Radiation Units and Measurements; 1989.
20. Hubbell JH, Seltzer SM. *Tables of X-Ray Mass Attenuation Coefficients and Mass Energy Absorption Coefficients from 1keV to 20MeV for Elements z=1 to 92 and 48 Additional Substances of Dosimetric Interest.* Gaithersburg, MD: National Institute of Standards and Technology, US Department of Commerce; 1996.
21. McMinn RMH, Hutchings RT, Logan BM. *Color Atlas of Head and Neck Anatomy.* Baltimore, MD: Mosby-Wolfe; 1995.
22. Kinahan PE, Townsend DW, Beyer T, Sashin D. Attenuation correction for a combined 3D PET/CT scanner. *Med Phys.* 1998;25:2046–2053.
23. Burger C, Goerres G, Schoenes S, Buck A, Lonn AHR, von Schulthess GK. PET attenuation coefficients from CT images: experimental evaluation of the transformation of CT into PET 511-keV attenuation coefficients. *Eur J Nucl Med Mol Imaging.* 2002;29:922–927.
24. White DR, Woodard HQ, Hammond SM. Average soft-tissue and bone models for use in radiation-dosimetry. *Br J Radiol.* 1987;60:907–913.
25. Nestor PJ, Fryer TD, Smielewski P, Hodges JR. Limbic hypometabolism in Alzheimer's disease and mild cognitive impairment. *Ann Neurol.* 2003;54:343–351.
26. Studholme C, Hill DLG, Hawkes DJ. An overlap invariant entropy measure of 3D medical image alignment. *Pattern Recognit.* 1999;32:71–86.
27. Kinahan PE, Rogers JG. Analytic 3D image reconstruction using all detected events. *IEEE Trans Nucl Sci.* 1989;36:964–968.
28. Mazziotta J, Toga A, Evans A, et al. A probabilistic atlas and reference system for the human brain: International Consortium for Brain Mapping (ICBM). *Philos Trans R Soc Lond B Biol Sci.* 2001;356:1293–1322.
29. Maldjian JA, Laurienti PJ, Kraft RA, Burdette JH. An automated method for neuroanatomic and cytoarchitectonic atlas-based interrogation of fMRI data sets. *Neuroimage.* 2003;19:1233–1239.
30. Kops ER, Herzog H. Template based attenuation correction for PET in MR-PET scanners. *IEEE Nucl Sci Symp Conf Rec.* 2008:3786–3789.
31. Klein A, Andersson J, Ardekani BA, et al. Evaluation of 14 nonlinear deformation algorithms applied to human brain MRI registration. *Neuroimage.* 2009;46: 786–802.
32. Lammertsma AA, Hume SP. Simplified reference tissue model for PET receptor studies. *Neuroimage.* 1996;4:153–158.
33. Ansorge RE, Sawiak SJ, Williams GB. Exceptionally fast non-linear 3D image registration using GPUs. *IEEE Nucl Sci Symp Conf Rec.* 2009:4088–4094.